The absence of nickel effect on iron isotope fractionation during core formation

E Kubik, P A Sossi, J Siebert, E Inglis, M Roskosz, E Siciliano Rego, N Wehr, F Moynier

The absence of nickel effect on iron isotope fractionation during core formation

E. Kubik[1], P.A. Sossi[1,2], J. Siebert[1,3], E. Inglis[1], M. Roskosz[4], E. Siciliano Rego[1,5,6], N. Wehr[1], F. Moynier[1].

[1]Université de Paris, Institut de Physique du Globe de Paris, CNRS, UMR 7154, 1 Rue Jussieu, 75005 Paris, France

[2]Institute of Geochemistry and Petrology, ETH Zürich, CH-8092 Zürich, Switzerland

[3]Institut Universitaire de France, Paris, France

[4]Institut de Minéralogie, de Physique des Matériaux, et de Cosmochimie (IMPMC), UMR CNRS 7590, Sorbonne Universités, Muséum National d'Histoire Naturelle, CP 52, 57 rue Cuvier, Paris F-75231, France.

[5]Instituto de Geociências, Universidade de São Paulo, Rua do Lago 562, Cidade Universitária, São Paulo, 05508-080, Brazil.

[6]Géosciences Montpellier, Université de Montpellier, CNRS, Université des Antilles, 34095, Montpellier, France.

Abstract

The mantellic Fe isotope compositions from differentiated inner solar system bodies are similar to, or heavier than chondritic meteorites. Core–mantle differentiation is a likely contributor to planetary isotopic fractionation. However, previous metal–silicate experiments provide only equivocal evidence for such fractionation, in which it has been argued that the Ni content of core-forming metal influences the extent of Fe isotopic fractionation. Here, we complement existing data with twenty-two novel metal–silicate equilibrium experiments with

varying Ni content to better quantify its effect on the vector and magnitude of Fe isotope fractionation during core formation. We find no statistically resolvable effect of the Ni content in the metallic phase on the Fe isotopic fractionation factor over a wide range of Ni concentrations (0 to 70 *wt.*% in the metal). In particular, the Fe isotopic composition of alloys from two experiments performed with 70 *wt.*% of Ni ($\delta^{56}Fe_{metal}$=0.27±0.01 and 0.32±0.01) are identical to the bulk experimental starting material (0.27±0.10). Our data across all experiments yield an average isotopic fractionation factor $\Delta^{56}Fe_{met–sil}$=0.05±0.11 (2σ) at 1873 K and 1–2 GPa, suggesting that little to no isotopic fractionation of Fe is expected to occur during core formation at low pressures. As such, our data does not support core formation as the main mechanism causing the observed variability in Fe isotope ratios between the silicate Earth, Moon, Vesta and other differentiated asteroids. A combination of multiple accretion-related processes—including condensation from the solar nebula, volatile-depleting events such as giant impacts, and disproportionation of ferrous iron to ferric iron and iron metal in larger bodies—as well as deep mantle and recycling processes could explain the heavier signatures in the silicate Earth and Moon. Furthermore, our results support the ideality of mixing among Fe–Ni alloys, previously demonstrated for physical properties but less conclusively evidenced for chemical properties.

Introduction

Experimental determination of isotopic fractionation of siderophile elements between metal and silicate has been used to investigate core formation on planetary bodies (e.g. Georg et al., 2007; Bourdon et al., 2018). Recorded experimental isotopic fractionations can be compared to natural isotope signatures, providing a powerful tool for interpretation of planetary isotope signatures and refining our knowledge of the history of solar system planetary bodies. In principle, a melted silicate and a melted metal are equilibrated at high pressure and high

49 temperature until elemental and isotopic equilibrium between the two phases is reached. The
50 silicate glass and metal grains from each quenched experiment are physically separated and
51 their isotope compositions are determined. Such studies on various siderophile elements can be
52 used to trace the conditions of planetary differentiation—its temperature (Hin et al., 2014), its
53 pressure (Labidi et al., 2016), redox conditions (Dalou et al., 2019), subsequent
54 rehomogenisation mechanisms (Kempl et al., 2013), and the composition of the core (Savage
55 et al., 2015; Mahan et al., 2017; Xia et al., 2019). Applied to elements presenting a volatile
56 behaviour, they open the possibility to trace the timing and origin of planetary volatile delivery
57 (Kubik et al., 2021). Such results allow the isotopic characterisation of the building blocks that
58 accreted into planetary bodies (Hin et al., 2014), permitting assessment of whether core
59 formation is the main planetary process controlling the abundances and isotope compositions
60 of certain elements in the accessible mantle of the body. Alternatively, other possible
61 mechanisms such as magmatic differentiation (Bonnand et al., 2016) or volatilisation processes
62 (Xia et al., 2019) may be required. Numerous key questions may thus be addressed through
63 experimental evidence. However, experimentally determined isotopic fractionation factors are
64 often in disaccord with one another, namely, Zn (Bridgestock et al., 2014; Mahan et al., 2017;
65 Xia et al., 2019), Si (Shahar et al., 2009,2011; Hin et al., 2014; Kempl et al., 2013), Ni (Lazar
66 et al., 2012; Guignard et al., 2020), Cu (Savage et al., 2015; Xia et al., 2019). These
67 discrepancies are partially attributable to differences in the experimental approach. In this
68 respect, replication of such experiments combined with independent, non-experimental
69 determination of the isotopic consequences of core formation (e.g. Georg et al., 2007; Moynier
70 et al., 2011) can only be beneficial to the general understanding of planetary differentiation.
71 Planetary materials show significant variability in Fe isotopic compositions. Ordinary,
72 enstatite and carbonaceous chondrites have an average δ^{56}Fe (per mil variation of the ^{56}Fe/^{54}Fe
73 ratio relative to IRMM-014) of 0.00±0.01‰ (2σ) (Craddock and Dauphas, 2011; Schoenberg

74 and von Blanckenburg, 2006; Wang et al., 2013, 2014). The terrestrial mantle is estimated to
75 have a $\delta^{56}Fe$=0.03±0.02‰ (Craddock et al., 2013; Sossi et al., 2016a; Weyer and Ionov, 2007)
76 while mid-ocean ridge basalts (MORB) are isotopically heavier with average
77 $\delta^{56}Fe$=0.10±0.01‰ (Teng et al., 2013; Craddock et al., 2013; Craddock and Dauphas, 2011;
78 Nebel et al., 2018; Weyer and Ionov, 2007). Even accounting for the effect of olivine
79 crystallisation and correcting their Fe isotopic composition back to that of a primary melt in
80 equilibrium with mantle peridotite, MORBs define an average $\delta^{56}Fe$=0.07±0.01‰ (Sossi et al.,
81 2016a; Nebel et al. 2018), heavier than chondritic meteorites. By contrast, primary melts of the
82 martian and vestan mantles, determined respectively from the SNC (shergottite-nakhite-
83 chassignite) and HED (howardite-eucrite-diogenite) groups of meteorites, have near-chondritic
84 isotopic signatures (Poitrasson et al., 2004; Schoenberg and von Blackenburg, 2006; Wang et
85 al., 2012; Sossi et al., 2016b) whereas angrites are markedly heavier ($\delta^{56}Fe$=0.12±0.04‰, n=7,
86 Wang et al., 2012). Lunar basalts yield a range of isotopic compositions from near-chondritic
87 to 0.3‰ (Weyer et al., 2005; Poitrasson et al., 2004; Liu et al., 2010; Wang et al., 2015; Sossi
88 and Moynier, 2017; Poitrasson et al., 2019), but ferroan anorthosites and Mg suite rocks from
89 the lunar highlands define an estimated bulk lunar Fe isotope composition similar to that of the
90 Earth's mantle ($\delta^{56}Fe$=0.05±0.03‰, Sossi and Moynier, 2017; Poitrasson et al., 2019).

91 Several processes have been proposed to account for this Fe isotopic variability
92 including (1) volatile loss by vaporisation during the Moon-forming giant impact (Poitrasson
93 et al., 2004; Poitrasson 2007; Liu et al., 2010), (2) accretion from the solar nebula associated
94 with various degrees of nebular or post-nebular Fe loss in planetary building blocks (Sossi et
95 al., 2016b), (3) disproportionation of ferrous iron (Fe^{2+}) into Fe^{3+} and metallic iron by
96 bridgmanite crystallisation during accretion in bigger planetary bodies such as the Earth
97 (Williams et al., 2012; Frost and McCammon, 2008), (4) core–mantle equilibration related
98 isotopic fractionation at either high (Polyakov, 2009) or low pressures (Elardo and Shahar,

2017) and (5) deep mantle recycling processes (Smith et al., 2021; Soderman et al., 2021). Lesher et al. (2020) argued that the upper part of the Earth's core could be enriched in heavier Fe isotopes by thermo-diffusion. If this isotopically heavier Fe is, as suggested in the study, transported to the upper mantle by ascending plumes, it could explain the heavy Fe isotopic signature of the BSE (bulk silicate Earth). However, core–mantle equilibration remains the largest chemical mass transfer process that occurred on Earth, suggesting that it may have also defined the observed isotopic signatures of its present-day core and mantle. It is therefore paramount to understand the isotopic behaviour of Fe during core–mantle equilibration.

However, the degree and direction of Fe isotope fractionation between silicate and core-forming alloy is influenced by a variety of variables. Early experimental work addressing this question did not find any resolvable Fe isotopic fractionation between S-free metallic and silicate phases over a range of pressures, from 1 to 60 GPa (Poitrasson et al., 2009; Hin et al., 2012; Shahar et al., 2015; Liu et al., 2017), leading to the conclusion that, at the high temperatures required for core formation on terrestrial bodies (≥ 2000 K, *e.g.,* Righter and Drake, 1996), equilibrium isotope fractionation between metal and silicate—which is proportional to $1/T^2$—should be negligible compared to the observed variations. Although some of the metallic phases investigated contained a small fraction of Ni (~5–9 *wt.*%) as is relevant to planetary cores, the effect of Ni on iron isotope fractionation was not explicitly investigated prior to the study of Elardo and Shahar (2017). They reported piston cylinder experiments conducted at 2123 K and 1 GPa in which the Ni content of the metal varied between 1 and 26 *at.*%, and observed a systematic increase of the isotopic fractionation factor with Ni content, which defines the following relation: $\Delta^{57}Fe_{met\text{-}sil}=0.011(Ni, at.\%)+0.04$. Thus, adding Ni to the metal phase enhances the Fe isotopic fractionation between metal and silicate, leading to an enrichment of the silicate in the lighter Fe isotopes relative to the metal. Because the sense of this isotopic fractionation is opposite to that observed in the mantles of differentiated bodies,

Elardo and Shahar, (2017) invoked significant isotopic fractionation during partial melting to restore the light subchondritic mantle isotopic composition inferred from their experiments to the superchondritic values observed in basaltic achondrites (*e.g.* Sossi et al. 2016a). Importantly, such an isotopic effect implies that Fe–Ni alloys do not mix ideally, which is at odds with the constancy of density, compressibility, and wave velocities of Fe–Ni alloys with increasing Ni content (*e.g.* Lin et al., 2003; Kantor et al., 2007; Martorell et al., 2013; Badro et al., 2014). Moreover, this ideality has been assumed in numerous experimental studies on core formation processes in which the effect of Ni was neglected. Xia et al. (2019) report Zn and Cu metal–silicate isotope fractionation experiments with significant sensitivity to the Ni content of the metal. Positive Ni-induced isotopic fractionations were measured for Fe (Elardo and Shahar, 2017), Zn and Cu (Xia et al., 2019), based on less than 10 experiments for each element. More experimental results, involving a broader range of Ni contents, are needed to establish whether there is a resolvable effect of the Ni content of an Fe–Ni alloy on various chemical and isotopic parameters. Therefore, assessing the Fe isotope fractionation between metal and silicate has profound implications for our understanding of core formation processes and for the physical and chemical properties of core-forming alloys.

To address this question, twenty-two novel metal–silicate equilibrium experiments were performed in order to characterise the effect of Ni on the Fe isotope fractionation. In particular, a wider range of Ni content in the metal (from 0 to 70 *wt.*%) was covered compared to previous studies (0 to 25 *wt.*%, Elardo and Shahar, 2017).

Method

Experimental method

Mixtures composed of 70 *wt.*% MORB with varying proportions of pure Fe and Ni were prepared by weighing each component and grinding them in an agate mortar until complete

148 homogenisation. All experiments were performed in a 150-ton end-loaded piston cylinder
149 apparatus at the Institut de Physique du Globe de Paris (IPGP), Université de Paris, in ½" talc
150 pyrex assemblies using graphite furnaces. Pressure calibration of the apparatus was performed
151 using the alumina concentration in orthopyroxene in equilibrium with pyrope in a MgO–Al_2O_3–
152 SiO_2 system (Perkins and Newton, 1981). The friction coefficients reported by McDade et al.
153 (2002) were compared and found to be identical to the coefficients measured during the
154 calibration of the apparatus, allowing similar corrections to be applied for friction loss for
155 assembly materials. During the experiments, the temperature was measured using a type D
156 ($W_{97}Re_3/W_{75}Re_{25}$) thermocouple contained in a 4-hole alumina sleeve just above the capsule
157 lid. Uncertainties on pressure and temperature are estimated to be around 0.1 GPa and 50 K
158 (Siebert et al. 2011). All experiments were performed at 1 to 2 GPa and at 1873 K in order to
159 induce complete fusion and promote equilibrium between metal and silicate in the system. Four
160 capsule types—boron nitride, crushable MgO, single-crystal MgO and graphite—were tested
161 in order to assess their effect on the Fe isotopic fractionation factor.

162 **Sample collection and purification**

163 The metal and silicate were separated mechanically after each experiment. Clean pieces
164 from each phase were selected carefully under magnifying glass. Metal pieces were directly
165 dissolved in 6 N HCl. Silicate samples were sorted in order to select clean pieces devoid of
166 metal bead or capsule material. These pieces were roughly crushed and a magnet was used to
167 remove any stray pieces of metal (Kubik et al., 2021). The silicate was finely crushed in an
168 agate mortar and digested in a 1:3 solution of HF:HNO_3 in closed Teflon bombs on a hotplate
169 at 100°C. Silicate samples were then dried and further digested in aqua regia on a hot plate at
170 150°C to remove any residual fluoride complex. They were dried again and dissolved in 6 N
171 HCl for purification. The purification of Fe in the samples was performed following the method
172 described in Sossi et al. (2015), by anion exchange chromatography using AG1-X8 (200-400

mesh) and 0.4 × 7 cm Teflon columns. Columns were filled with 1 mL AG1-X8 resin and cleaned with 5 mL 3 N HNO_3, 5 mL H_2O and conditioned with 5 mL 6 N HCl. The samples were subsequently loaded in 0.5 mL of 6 N HCl. The matrix was eluted with 11 mL of 6 N HCl. The Fe cuts were eluted with 3 mL of 0.5 N HCl, and dried to be redissolved in 0.5 N HNO_3. They were diluted to 4 ppm Fe solutions and spiked with 8 ppm of Ni, following the method described in Sossi et al. (2015).

MC-ICPMS measurements

Iron isotopic measurements were performed on a Neptune Plus MC-ICPMS at IPGP (Université de Paris), used in medium resolution mode. The cups were configured as described in Sossi et al. (2015) in order to collect the intensity on the masses 53, 54, 56, 57, 60 and 61. The mass 53 was used to correct for any ^{54}Cr interference on ^{54}Fe, even though chromatographic separation was shown to be very efficient, meaning the correction was insignificant. The $^{61}Ni/^{60}Ni$ ratios measured in all samples were used to correct for mass bias effects. Measurements of IRMM-014 performed in between samples were used to calculate the delta values reported in this study. International reference materials were measured along with the experimental samples with Fe isotopic compositions reproducing the previously published values (*e.g.* for BHVO-2: $\delta^{56}Fe=0.103\pm0.04$, 2 *s.d.*).

Evidence of metal–silicate equilibrium

Two methods are typically used in order to assess metal–silicate isotopic equilibrium in high-temperature experiments: time series and the "three-isotope method". It has been known for a few decades that elemental equilibrium can be reached very quickly at superliquidus condition in metal–silicate experiments (5 seconds at 2300 K, Thibault and Walter, 1995). As these diffusion rates cannot necessarily be extrapolated to the isotopic exchange rate, several experimental studies report that isotopic exchange can actually be faster than chemical diffusion while pointing to differences between systems (Lesher et al., 1990; Van der Laan, 1994). In this

context, numerous studies report relatively short equilibration time experiments (e.g. Hin et al., 2013; Kubik et al., 2021; Poitrasson et al., 2009; Shahar et al., 2011). The attainment of isotopic equilibrium after a few minutes can be explained by the superliquidus temperatures reached, at which the entire sample is melted. The molten state promotes equilibration because (1) diffusion rates are significantly higher in the liquid state than in presence of a solid phase, (2) convection further stirs the melt inside the capsule, owing to the small thermal gradient endemic to high pressure experiments, (3) homogenisation is additionally favoured by using a finely crushed powder as a starting material. Time series experiments are an empirical way to establish the time needed to achieve equilibrium. In this study specifically, (a) thorough SEM and EDX characterisation of each phase allowed to provide proof that the entirety of the sample material was fully molten and (b) resulted in chemically homogeneous phases (see supplementary information). (c) The Fe isotopic fractionation factors follow a systematic trend that can be statistically determined to good precision due to an extensive data set comprising 22 experiments. (d) Repeated time series experiments show no statistically resolvable evolution of the Fe isotopic fractionation factor between runs of 3- and 30-minute duration (see supplementary information), with experiments of 30 minutes and more exhibiting greater variability, with both positive and negative isotopic fractionation factors observed. This is attributed to progressive reaction of the silicate melt with the capsule material over time. Moreover, the results reported in this study are in agreement with several other studies performed in a range of laboratory facilities with different methodologies and apparatuses (Poitrasson et al., 2009; Hin et al., 2012; Liu et al., 2017; Elardo and Shahar, 2017, Fig. 1a). The results from our study are also in agreement with numerous pieces of evidence of Fe–Ni alloy ideality (Lin et al., 2003; Kantor et al., 2007; Martorell et al., 2013; Badro et al., 2014; Huang and Badro, 2018). With respect to demonstration of isotopic equilibrium, the three-isotope method was not included in the protocol of this study. Although Cao and Bao (2017)

and Bourdon et al. (2018) reported artifacts that could induce non-linear trajectories, leading the authors to delineate limitations of the method, other studies have argued for its robustness (Shahar et al., 2008; Shahar and Young, 2020), and in particular its usefulness in verifying that the system remained closed with respect to mass exchange throughout an experiment. In this study, the use of single-crystal MgO capsules was employed to ensure minimal chemical and isotopic interaction with the capsule (see supplementary information). Moreover, the recalculation of the bulk isotope composition of the experiments based on measured $\delta^{56}Fe$ of each phase by mass balance yields a good reproducibility (on average $\delta^{56}Fe_{bulk}$=0.40±0.08‰, 1 s.d.). The three-isotope method is predicated on experiments that preserve a record of the approach to equilibrium between two phases, and thus represent a form of time-series in which equilibration times are necessarily slow. Because equilibrium is achieved within a few minutes in our experiments, the three-isotope method is unfeasible from an experimental standpoint. Namely, the timescale of equilibration of the piston cylinder assembly to ensure stable conditions (*e.g.*, Matjuschkin et al., 2015) is of the same order of that required for the three-isotope method to produce dispersion in isotope composition. Each bulk starting material used in this study was also measured for Fe isotopes and are found to reproduce the calculated bulk value within error for 12 of them which further supports closed system and equilibrium achievement.

Iron isotopic behaviour in metal–silicate equilibrium experiments

Twenty-two metal–silicate equilibrium experiments were performed at 1 and 2 GPa and 1973 K. Run durations were varied between 3 and 60 minutes in order to assess the timescales required to approach isotopic equilibrium. Petrographic observations indicate that the starting material was fully molten in all experiments (see supplementary materials). The metal coalesced into a discrete sphere in most experiments, and subsequent to quenching, was

separated mechanically from the silicate phase. All experimental parameters and isotopic measurements are available in Table 1.

Iron isotope fractionation results for all experiments from this study and literature are presented in Fig. 1a. It should be noted that experiments from other studies were carried at different temperature conditions and were therefore recalculated at 1873 K for comparison with the dataset reported herein by using the relationship $\Delta^{56}Fe_{metal-silicate} = a \cdot \frac{1}{T^2}$ (*e.g.* Urey, 1947). Our results show no correlation between the Ni content of the metal and the Fe isotopic fractionation factor between metal and silicate (Fig. 1b). There is also no resolvable difference between the experiments using the different types of capsules, although from petrographic observations single-crystal MgO capsules minimise the extent of reaction between capsule and sample by containing the interactions within the first 30 µm of the capsule. Isotope measurements on multiple parts of experiment E375 are presented in Fig. 2. This short-duration experiment exhibits a glassy silicate in the center and partially crystallised silicate towards the capsule boundary where skeletal olivine crystals grew as a result of MgO enrichment and the relatively low quenching rates achievable in the piston cylinder (*e.g.* Green et al., 1975). Measurements on these separated parts show no difference in Fe isotopic composition between glass and crystallised silicates (δ^{56}Fe=0.30±0.03‰ and 0.29±0.05‰ respectively) which means that MgO diffusion towards the center of the sample does not affect the Fe isotope composition of the silicate. Therefore, in this particular case, MgO capsules are well-suited for isotope fractionation experiments with respect to MgO diffusion. This experiment also presents an isotopic composition of the metal identical to the silicate. The first 30 µm of the capsule in contact with the melt contains less than 4 *wt.*% of Fe, however, exhibits a clear enrichment in light Fe isotopes, even after a few minutes. At such superliquidus temperatures, chemical reactions between the capsule and the sample progress with increasing run duration. Therefore,

in the long term, measured isotopic fractionations can be driven by interactions between the capsule and the sample.

Iron isotopic fractionation factors from this study yield an average of $\Delta^{56}Fe_{met\text{-}sil}$=0.05±0.11‰. This means that these results are not significantly different from 0.0‰, and no dependence on the Ni content of the metal is detected over a wide range of Ni concentrations.

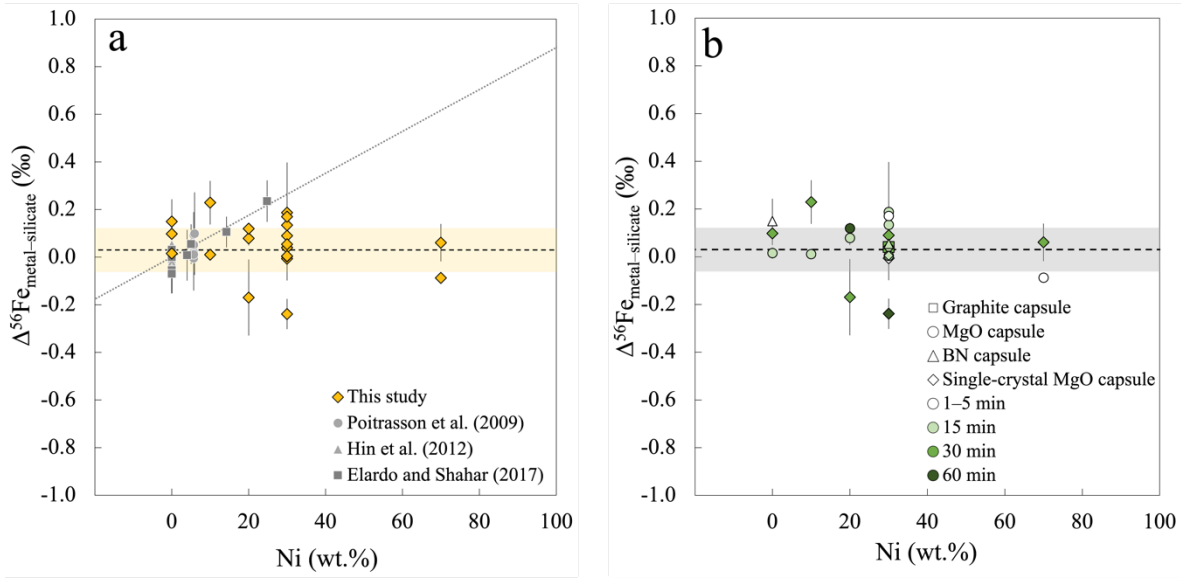

Figure 1: Results of Fe isotopic fractionation in metal–silicate equilibrium experiments. Error bars correspond to 2 standard deviations. **a.** $\Delta^{56}Fe_{metal-silicate}$ of all experiments of this study and from literature recalculated at 1873 K (Poitrasson et al., 2009; Hin et al., 2012; Elardo and Shahar, 2017) as a function of the Ni content of the metallic phase. The horizontal dashed line with orange error represents the average of all experiments presented on the graph, *i.e.* 0.03±0.09‰ (1 s.d.). The dotted line represents the trend of Ni content dependency on Fe isotopic fractionation factor determined by Elardo and Shahar (2017). **b.** $\Delta^{56}Fe_{metal-silicate}$ for all experiments of this study. Squares are experiments carried in graphite capsules, circles correspond to the ones in crushable MgO capsules, triangles for experiments using boron nitride capsules and diamonds for experiments carried in single-crystal MgO capsules. Experiments are color coded according to their time durations: white for 1-5 minutes, pale green for 15 minutes, light green for 30 minutes, and dark green for 60 minutes. The horizontal dashed line with grey error represents the average of all experiments presented on graph a., *i.e.* 0.03±0.09‰ (1 s.d.).

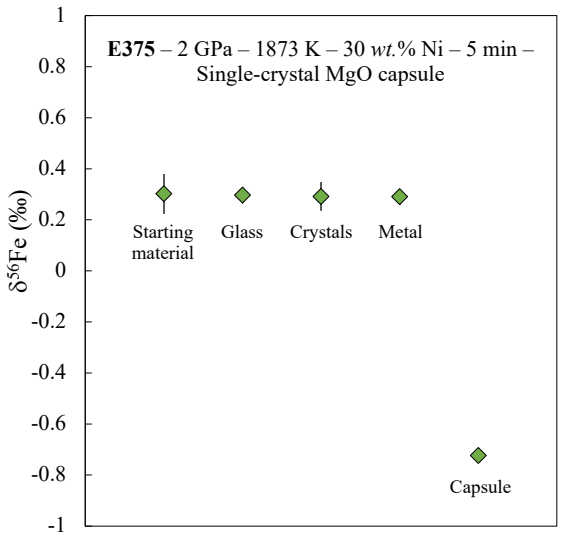

Figure 2: Results of Fe isotopic compositions on a single experiment. E375 was performed at 2 GPa and 1873 K in a single-crystal MgO capsule with a time duration of 5 minutes. Its metal phase contains 5 *wt.*% of Ni. Iron isotopic measurements were performed on two silicate samples—a central glassy part and an outlying crystallised part—as well as the metal phase and the capsule. The two silicate parts and the metal present identical isotopic composition to the starting material whereas the inner part of the capsule (inner 30 μm) is enriched in light Fe isotopes. The diffusion of MgO from the capsule has no effect on the Fe isotopic composition of the silicate phase.

The Fe isotope compositions of the bulk starting materials were measured to assess potential Fe loss during the experiments (Table 1). These measured Fe isotope compositions of the starting material were compared to bulk values calculated by mass balance from the Fe isotopic composition of the metal and silicate from the run products (Fig. 3). Although there is no clear correlation between the fractionation factor and the agreement between the measured and calculated bulk values, both estimations of the bulk experimental Fe isotope composition coincide within error for 12 out of the 22 experiments of the reported data set. This indicates that experiments largely approached closed system behaviour, resulting in limited loss of Fe through the capsule. Thorough characterisation of the Fe content of experimental capsules after the experiments showing moderate Fe diffusion into the capsules also corroborates closed system behaviour, a necessary condition to properly investigate isotope fractionation processes experimentally. Iron loss quantified by the difference between the measured and calculated bulks shows that single-crystal MgO capsules present reduced Fe loss with respect to other capsule types (Supplementary Fig. 9).

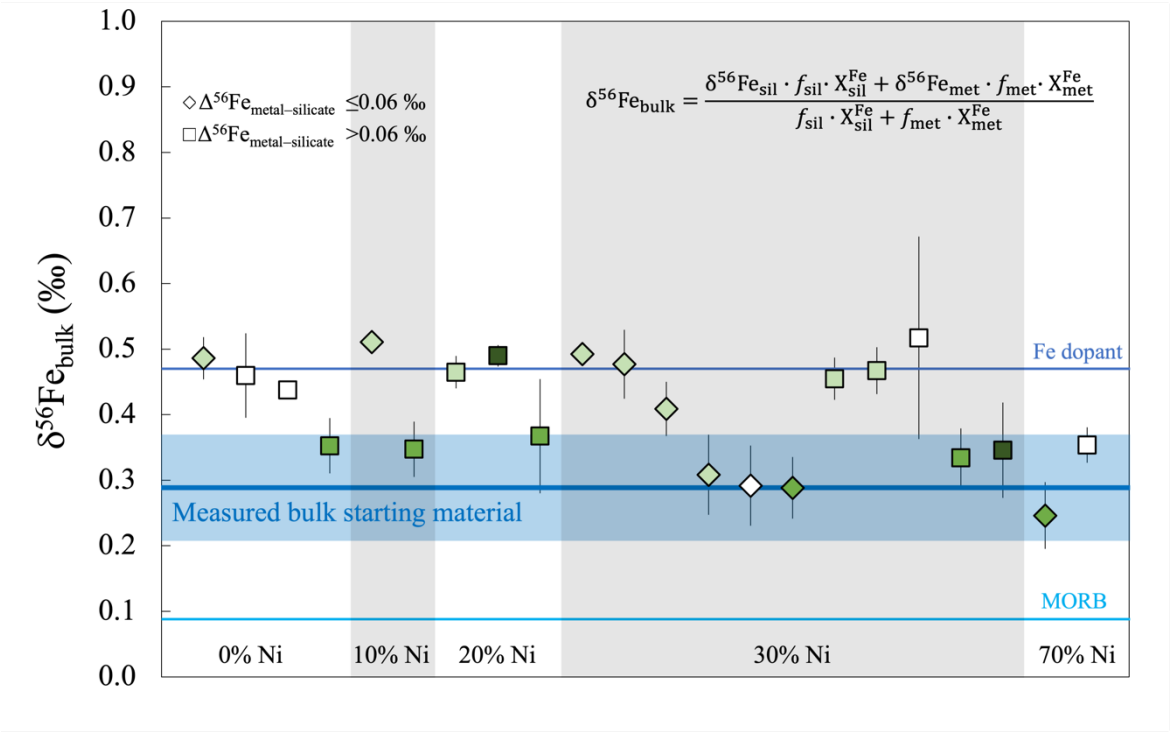

Figure 3: Comparison of measured and calculated Fe isotope compositions of bulk experiments. The blue line represents the average Fe isotope composition measured from the powder mixtures used as starting materials in the experiments. The symbols correspond to calculated Fe isotope compositions of bulk experiments from mass balance using metal and silicate Fe isotopic measurements for each experiment (equation on the figure). Squares are used for experiments presenting a metal–silicate fractionation factor superior to 0.06‰ and unfractionated experiments correspond to diamonds. Computed bulk value symbols are color-coded according to the run duration: white for 1–5 min, pale green for 15 min, light green for 30 min and dark green for 60 min.

Fig. 4 displays the Fe isotope composition of single experimental phases from this study and Elardo and Shahar (2017) as a function of metal Ni content. The Ni-induced Fe isotope fractionation proposed by Elardo and Shahar (2017) implies that such a fractionation is driven by the composition of the metallic phase as Ni is predominantly hosted in the metallic phase. Therefore, a clear variation of the metal Fe isotope composition should be observed as a function of the metal Ni content. However, no systematic change in the metal Fe isotope composition is reported in the data set from this study (Fig. 4a). In fact, the composition of both experiments performed with 70 *wt.*% of Ni ($\delta^{56}Fe_{metal}$=0.27±0.01 and 0.32±0.01) are strictly identical to the measured bulk experimental starting material (0.27±0.10, 2σ). It should be noted that these two experiments also underwent negligible Fe loss (Fig. 3). This constitutes strong evidence for a very limited effect of Ni on the Fe isotope fractionation at the experimental

conditions of this study. The silicate Fe isotope compositions present a more scattered distribution (Fig. 4b), likely due to moderate interactions with the capsule, and equally show no correlation with the metal Ni content. Iron isotope compositions of single experimental phases from Elardo and Shahar (2017) show clear correlation with the Ni content (Fig. 4c and d). However, this is due to the fact that the silicate fraction of the starting mixtures was spiked with ^{54}Fe, resulting in starting materials with variable Fe isotope compositions with respect to their Ni content (Fig. 4c and d). The observed trends therefore reflect the evolution of the starting material rather than a metal–silicate isotope fractionation. We speculate that if this effect could be corrected by recalculating all the experiments for the same bulk starting material composition (by using the precise proportions of each component and/or Fe isotope compositions of starting materials as reported in our study), an effect of Ni content on the Fe isotope composition may not be detectable. Based on thorough study of comprehensive literature data and the novel experimental metal–silicate data set reported in this study, we conclude that there is no evidence for Ni-induced Fe isotope fractionation between metal and silicate.

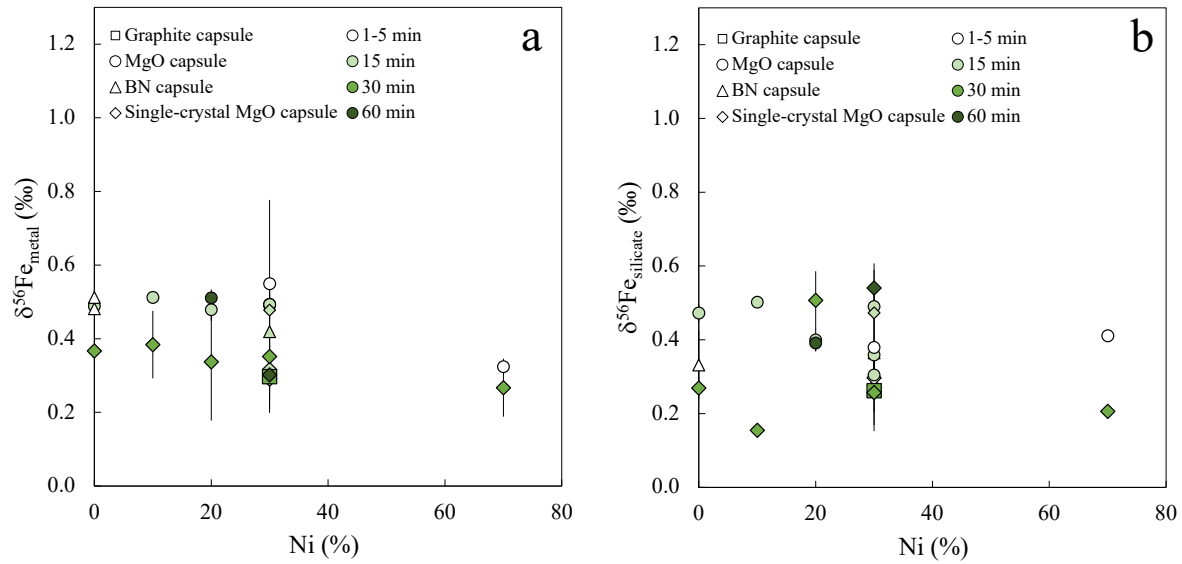

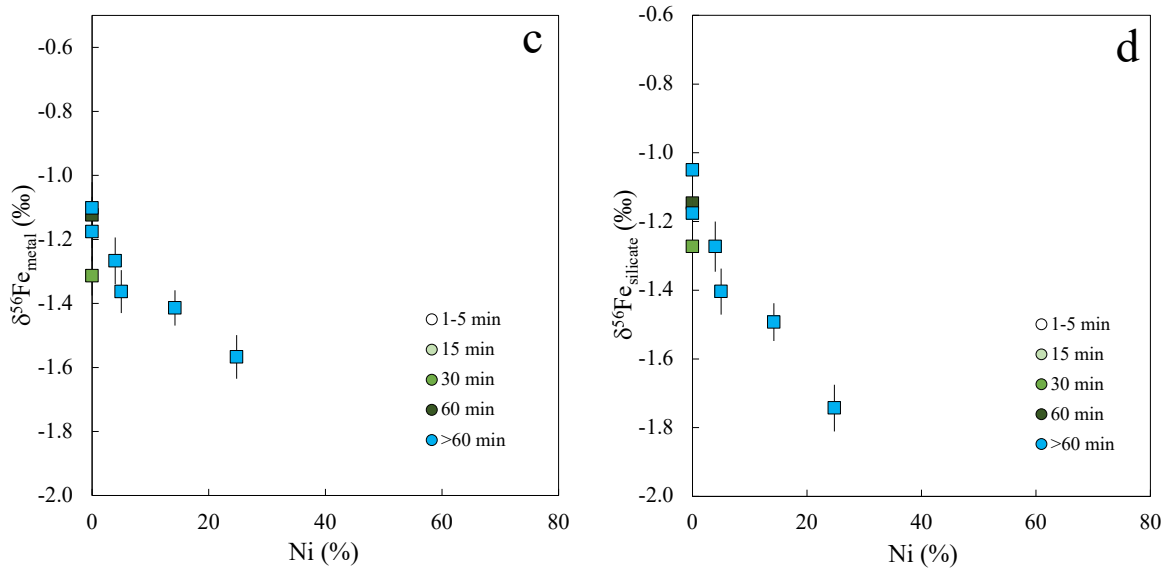

Figure 4: Iron isotope composition of separate phases from experiments reported in this study and Elardo and Shahar (2017) as a function of the metal Ni content. **a.** Iron isotope composition of metal phases from this study. **b.** Iron isotope composition of silicate phases from this study. **c.** Iron isotope composition of metal phases from Elardo and Shahar (2017). **d.** Iron isotope composition of silicate phases from Elardo and Shahar (2017).

Table 1: Iron isotopic compositions of experimental run products and experimental parameters as well as compositions of all starting materials used this study. Replicated samples were split before column separation.

Run	P (GPa)	T (K)	Ni (wt.%)	Time (min)	Capsule	$\delta^{57}Fe_{silicate}$	2σ	$\delta^{57}Fe_{metal}$	2σ	$\Delta^{57}Fe_{met-sil}$	2σ	$\delta^{56}Fe_{silicate}$	2σ	$\delta^{56}Fe_{metal}$	2σ	$\Delta^{56}Fe_{met-sil}$	2σ
E269	1	1873	20	15	MgO	0.61	0.03	0.73	0.02	0.12	0.03	0.40	0.02	0.48	0.01	0.08	0.02
E270	1	1873	10	15	MgO	0.75	0.01	0.78	0.04	0.02	0.01	0.50	0.01	0.51	0.03	0.01	0.01
E271	1	1873	20	60	MgO	0.60	0.02	0.77	0.03	0.17	0.02	0.39	0.01	0.51	0.01	0.12	0.01
E276	1	1873	30	15	MgO	0.46	0.03	0.73	0.06	0.27	0.03	0.30	0.03	0.49	0.05	0.19	0.03
E298	2	1873	30	15	MgO	0.78	0.02	0.75	0.02	-0.02	0.02	0.49	0.01	0.49	0.01	0.00	0.01
E302	2	1873	0	15	MgO	0.72	0.02	0.75	0.05	0.04	0.02	0.47	0.03	0.49	0.04	0.02	0.03
E318	2	1873	30	15	SC MgO	0.65	0.07	0.68	0.05	0.03	0.07	0.47	0.05	0.48	0.04	0.00	0.05
E320	2	1873	0	3	BN	0.50	0.09	0.71	0.03	0.21	0.09	0.33	0.06	0.48	0.03	0.15	0.06
E321	2	1873	30	15	BN	0.57	0.07	0.64	0.02	0.07	0.07	0.36	0.04	0.42	0.08	0.05	0.04
E322	2	1873	30	15	MgO	0.52	0.04	0.70	0.08	0.17	0.04	0.36	0.03	0.49	0.05	0.13	0.03
E323	2	1873	0	3	BN	0.54	0.07	0.77	0.01	0.23	0.07	0.00	0.00	0.51	0.00	0.00	0.00
E324	2	1873	30	3	MgO	0.58	0.16	0.78	0.16	0.20	0.16	0.38	0.11	0.55	0.11	0.17	0.11
E325	2	1873	70	3	MgO	0.59	0.01	0.47	0.02	-0.12	0.01	0.41	0.02	0.32	0.01	-0.09	0.02
E373	2	1873	30	15	SC MgO	0.43	0.02	0.44	0.09	0.01	0.11	0.28	0.02	0.32	0.04	0.04	0.06
E375 glass	2	1873	30	5	SC MgO	0.40	0.05	0.41	0.04	0.01	0.09	0.30	0.03	0.29	0.03	-0.01	0.06
E375 crystals						0.46	0.05					0.29	0.05				
E375 capsule						-1.07	0.07					-0.72	0.01				
E376	2	1873	30	30	SC MgO	0.43	0.03	0.48	0.00	0.05	0.03	0.26	0.03	0.35	0.02	0.09	0.04
E377	2	1873	70	30	SC MgO	0.25	0.04	0.43	0.07	0.14	0.08	0.21	0.04	0.26	0.02	0.06	0.05
E377 replicate								0.43	0.07					0.27	0.02		
E378	2	1873	0	30	SC MgO	0.40	0.07	0.50	0.01	0.15	0.05	0.28	0.05	0.37	0.02	0.10	0.04

E378	replicate						0.34	0.05					0.23	0.03				
E379		2	1873	10	30	SC MgO	0.21	0.05	0.55	0.04	0.35	0.09	0.15	0.02	0.38	0.02	0.23	0.04
E380		2	1873	20	30	SC MgO	0.73	0.08	0.50	0.08	-0.23	0.16	0.51	0.04	0.34	0.04	-0.17	0.09
E381		2	1873	30	30	graphite	0.38	0.02	0.41	0.01	0.03	0.03	0.26	0.02	0.30	0.02	0.04	0.05
E382		2	1873	30	60	SC MgO	0.81	0.00	0.44	0.06	-0.37	0.06	0.54	0.03	0.30	0.05	-0.24	0.07

Material	n	δ^{57}Fe	2σ	δ^{56}Fe	2σ
Fe dopant	5	0.69	0.06	0.47	0.08
MORB	5	0.11	0.08	0.09	0.05
Fe-Ni$_0$	4	0.47	0.24	0.33	0.10
Fe-Ni$_{10}$	4	0.45	0.14	0.28	0.04
Fe-Ni$_{20}$	4	0.38	0.17	0.26	0.03
Fe-Ni$_{30}$	4	0.45	0.23	0.30	0.08
Fe-Ni$_{70}$	4	0.42	0.20	0.27	0.10

Iron isotopic fractionation during core formation

Our experimental results include novel metal–silicate equilibrium Fe isotope fractionation data with a wide range of Ni content. The large number of experiments in this study provides enhanced statistical accuracy and shows that Ni proportion in the metal has a limited effect on the Fe isotope fractionation between metal and silicate. While our conclusions may differ, the results presented here are consistent (Fig. 1a) with those reported in the study of Elardo and Shahar (2017) where the observed trend can be attributed to a relatively smaller number of experiments. In fact, the data presented herein, combined with that of Elardo and Shahar (2017) yields an average fractionation factor of $\Delta^{56}Fe_{met\text{-}sil}$=0.04±0.11‰, indicating no isotopic fractionation within uncertainty. Our results are also in agreement with previous experimental studies on Fe isotopic fractionation (Poitrasson et al., 2009; Hin et al., 2012; Liu et al., 2017) demonstrating the absence of Fe isotope fractionation at metal–silicate equilibrium. Significant S contents in the alloy may induce a positive metal–silicate isotope fractionation with light isotope enrichment in the silicate (Shahar et al., 2014; Liu et al., 2017; Pinilla et al., 2021). A similar trend of isotopic fractionation has been observed for other elements such as Si and C (Elardo et al., 2019; Shahar and Young, 2020). Nevertheless, this vector of Fe isotopic

fractionation is opposite to that observed in Earth's mantle and in the mantles of other differentiated bodies relative to chondrites. Moreover, iron meteorites present Fe isotopic signatures heavier than chondrites by 0.1–0.2 ‰ (δ^{57}Fe) (*e.g.* Williams et al., 2006), preventing to explain heavy signatures in planetary mantles from differentiation of chondritic material. Instead, the heavy signatures observed in iron meteorites have been explained by core crystallisation with significant Fe isotopic fractionation measured experimentally between solid and liquid iron alloys (Ni et al., 2020; Young 2021). As such, to a first order there is no direct evidence for core–mantle segregation to cause significant isotopic fractionation of Fe in controlling the isotopic composition of planetary mantles. Indeed, equilibrium isotope fractionation depends on $1/T^2$ so that enhanced fractionation is expected from low temperature core formation. However, chondritic values are observed in small bodies that underwent lower temperature core formation such as Mars and Vesta (~1900 K, Righter and Drake, 1996) compared to the non-chondritic Earth whose core equilibrated with the mantle at 2500–3500 K (Wood et al., 2006). Therefore, core formation cannot explain alone the diversity of Fe isotope compositions in the inner solar system, although it has been previously proposed from in situ diamond anvil cell experiments coupled to nuclear resonant inelastic X-ray scattering measurements (Polyakov, 2009).

Planetary iron isotopic variability

Core formation as the main process responsible for Fe isotopic variability among planetary mantles is not well supported by the experimental results of this study. Other processes including various accretion and deep mantle mechanisms need to be further investigated as potential causes for the Fe isotopic variability between inner solar system planetary bodies.

Investigating the differences in Fe isotope signatures between the Earth and the Moon, an increasing amount of stable isotopic measurements on lunar rocks suggest that both bodies

391 share a common signature (Wang et al., 2015; Sossi and Moynier, 2017; Poitrasson et al., 2019),
392 while isotopic differences are only observed among volatile elements that were depleted from
393 the Moon. This result is in agreement with the widely held view that volatilisation during Moon
394 formation and evolution resulted in isotopic fractionation of multiple isotopic systems in the
395 lunar mantle on a much larger scale than in Earth's mantle (*e.g.* Gargano et al., 2020; Kato et
396 al., 2015; Pringle and Moynier, 2017; Sharp et al., 2010; Sossi et al., 2017, 2018; Wang and
397 Jacobsen, 2016). The observation of isotopically heavy Fe isotope signatures in ureilites and
398 angrites suggests that collisions between accreting bodies in the inner solar system may be
399 common and that the observed signatures in inner planetary bodies are the result of contrasted
400 accretional histories possibly involving multiple complex volatile-depleting events (Sossi et al.,
401 2016b). The corollary states that Mars and Vesta suffered very limited syn- and post-accretion
402 Fe loss as inferred from their chondritic signatures. The crystallisation of bridgmanite in large
403 planetary bodies such as the Earth may enrich the mantle in heavy Fe isotopes (Williams et al.,
404 2012) by disproportionation of Fe^{2+} into Fe^{3+} and metallic iron. Because metallic iron is
405 isotopically lighter than ferric iron-bearing bridgmanite, its sequestration into Earth's core
406 could produce a heavy Fe signature in the mantle without invoking volatilisation processes.
407 Note however that such effects have not been confirmed so far by *in situ* NRIXS measurements
408 and modelling of lower mantle crystallisation (Yang et al., 2019). Furthermore, this process
409 would not explain the heavy isotope compositions of achondritic meteorites whose parent
410 bodies were too small to have stabilised bridgmanite or Fe^{3+}-rich silicate melt (Armstrong et
411 al., 2019) in equilibrium with iron metal. Therefore, taken together, the aforementioned
412 mechanisms provide possible means to explain the diverse Fe isotope signatures observed
413 amongst inner solar system bodies.

414 Lesher et al. (2020) argued that the core–mantle boundary could be enriched in the
415 heavier Fe isotopes and that pockets of this heavy core could be entrained in plumes towards

the upper mantle and crust. High temperature diffusion experiments over a thermal gradient of 250ºC could provide a mechanism for the enrichment of the outer core and lowermost mantle in heavy Fe isotopes. This process is predicted to be slower than the mantle convection and recycling according to the study. Therefore, the proposed mechanism to transport heavier Fe core diapirs in magmatic plumes towards the upper mantle could be tested by measurements on OIBs spanning a wide age range. Although a subsequent study on OIBs does not support core liquids entrainment as the source of observed heavy OIB signatures (Soderman et al., 2021), the authors present a variety of potential processes explaining Fe isotopic variations in the mantle (*e.g.* subduction processes, hydrothermal alteration, contribution from sediments, peridotite and pyroxenite melting). Three main processes contributing to the establishment of heavy Fe isotope signatures in magmatic rocks are identified: (1) processes enriching eclogite in heavy Fe isotopes such as metamorphism, (2) lithospheric processing and (3) melting processes in conditions preventing the dilution of heavy Fe isotope-enriched melts with lighter isotope-enriched materials (Soderman et al., 2021). Diamond metallic inclusions presenting heavy signatures (Smith et al., 2021) that could not be explained by iron disproportionation were also proposed to originate from deep recycling processes. Despite the propensity for these processes to generate isotopic variability locally, they are incapable of shifting the composition of the entire mantle over geological time. This conclusion is founded on the observation of the constancy in the Fe isotope compositions of komatiites through time (Hibbert et al. 2012; Dauphas et al. 2010), and their concordance with those of peridotites that reflect the modern-day mantle (*e.g.* Weyer and Ionov, 2007).

On ideality in Fe–Ni alloys

The amount of Ni in the core is estimated to be around 5 *wt.*% based on geochemical and cosmochemical models (McDonough and Sun, 1995). Numerous studies show that physical properties such as density, compressibility, and wave velocities in Fe–Ni alloys vary only

441 marginally as a function of their Ni content (e.g., Lin et al. 2003; Kantor et al. 2007; Asker et
442 al., 2009; Martorell et al. 2013; Wakamatsu et al., 2018). Importantly, the constant density of
443 such alloys does not uniquely constrain the amount of Ni in the core but implies that the entirety
444 of the observed density deficit must be due to the presence of ~10% of light elements in the
445 core (Birch, 1952). Although the insensitivity of the physical properties of Fe–Ni alloys to the
446 Ni content has been verified from multiple experimental studies (Lin et al., 2003; Kantor et al.,
447 2007) and *ab initio* calculations (Martorell et al., 2013), this does not necessarily hold for their
448 chemical properties.

449 Presently, studies investigating experimentally the elemental and isotopic behaviour of
450 elements between metal and silicate which have considered the effect of the amount of Ni in
451 the metal are very scarce, largely because it has been widely assumed to be negligible for the
452 conditions relevant to core formation. Through the transpiration method and integration of the
453 Gibbs-Duhem relation, early studies illustrated that the dissolution of Ni had little effect on the
454 activity of Fe in binary alloys (Oriani, 1953; Zellars et al. 1959). As such, it is frequently
455 assumed that the alloying of Fe with small quantities of Ni has a negligible effect on the
456 behaviour of the metal. More recent Knudsen effusion mass spectrometric investigations of the
457 activity-composition relations of liquid Fe–Ni alloys (Fraser and Rammensee, 1982) show that
458 the activity coefficient of Fe, γFe, varies between 0.9 at X_{Ni}=0.5 to 1 at X_{Ni}=0.05 (X=mole
459 fraction), highlighting that for all likely core compositions, Fe dissolution in Fe–Ni alloys is
460 ideal at ambient pressures. At higher pressures (up to 94 GPa), Huang and Badro (2018)
461 demonstrated that Ni (between 3.5 to 48.7 *wt.*% Ni) has no effect on the metal–silicate
462 partitioning of Ni, Cr and V. Our study suggests that the Ni fraction in an Fe–Ni alloy has no
463 effect on Fe isotopic behaviour in a metal–silicate equilibrium, also pointing towards chemical
464 Fe–Ni ideality. Xia et al. (2019) report contrasting observations, in which the magnitude of Zn
465 and Cu isotope fractionation between metal and silicate was shown to be sensitive to the Ni

content of the alloy, which could be due to specific interactions between Ni and these elements. The 22 experiments reported herein not only enhance statistical accuracy but were also designed to explore a much broader range of Ni concentrations in the metal, from 0 to 70 *wt.*% (~25 *wt.*% maximum in Xia et al., 2020 and Elardo and Shahar, 2017). The assumption of chemical Fe–Ni ideality has extended implications regarding our understanding and knowledge of core formation related processes.

Conclusion

We performed 22 metal–silicate equilibrium experiments with the objective of establishing the effect of Ni content of Fe–Ni alloys on the Fe isotope fractionation factor between metal and silicate. All experiments were carried out at 1–2 GPa and 1873 K, at which a variety of capsule materials were tested. An experimental time series, as well as petrographic characterisations of the samples were performed in order to assess the conditions at which chemical equilibrium was achieved. No significant effect of Ni concentration on Fe isotope fractionation was detected over a wide range of Ni contents (0–70 *wt.* % in the metal fraction), supporting the common assumption of physical and chemical ideality of Fe–Ni alloys. Because the observed fractionation factor between metal and silicate is indistinguishable from zero, our data does not support core formation as the main mechanism causing the diversity in Fe isotope signatures observed amongst inner solar system planetary bodies. A combination of multiple accretion-related processes—including condensation from the solar nebula, volatile-depleting events such as giant impacts, and disproportionation of ferrous iron by bridgmanite crystallisation in larger bodies—as well as deep mantle and recycling processes, could together contribute to the observation of heavier-than-chondritic signatures in the Earth and the Moon's mantles.

Acknowledgement

We thank Stephan Borensztajn for technical support at the SEM platform. The authors thank Pascale Louvat for her support and indispensable expertise at the MC-ICPMS platform. The authors acknowledge the financial support of the UnivEarthS Labex program at Sorbonne Paris Cité (ANR-10-LABX-0023 and ANR-11-IDEX-0005-02). Part of the work was supported by IPGP multidisciplinary program PARI, by Région Île-de-France SESAME Grants no. 12015908, EX047016 and the IdEx Université de Paris grant, ANR-18-IDEX-0001 and the DIM ACAV+. JS acknowledges the financial support of the French National Research Agency (ANR Project VolTerre, grant no. ANR-14-CE33-0017-01). FM acknowledges funding from the European Research Council under the H2020 framework program/ERC grant agreement METAL. ER acknowledges funding from Fundação de Amparo à Pesquisa do Estado de São Paulo (FAPESP grant 2019/16271-0; 2018/05892-0).

References

K. Armstrong, D.J. Frost, C.A. McCammon, D.C. Rubie, T. Boffa Ballaran, 2019. Deep magma ocean formation set the oxidation state of Earth's mantle. Science 365, 903-906.

C. Asker, L. Vitos, I.A. Abrikosov, 2009. Elastic constants and anisotropy in FeNi alloys at high pressure from first-principle calculations. Phys. Rev. 79, 214112.

J. Badro, A. S. Cote, and J. P. Brodholt, 2014. A seismologically consistent compositional model of Earth's core. Proc. Natl. Acad. Sci., 111(21):7542–7545.

F. Birch, 1952. Elasticity and constitution of the Earth's interior. J. Geophys. Res., 57(2):227–286.

P. Bonnand, H. Williams, I. Parkinson, B. Wood, and A. Halliday, 2016. Stable chromium isotopic composition of meteorites and metal–silicate experiments: Implications for fractionation during core formation. Earth Planet. Sci. Lett., 435:14–21.

B. Bourdon, M. Roskosz, and R. C. Hin, 2018. Isotope tracers of core formation. Earth Science Rev., 181(April):61–81.

L. J. Bridgestock, H. Williams, M. Rehkämper, F. Larner, M. D. Giscard, S. Hammond, B. Coles, R. Andreasen, B. J. Wood, K. J. Theis, C. L. Smith, G. K. Benedix, and M. Schönbächler, 2014. Unlocking the zinc isotope systematics of iron meteorites. Earth Planet. Sci. Lett., 400:153–164.

X. Cao and H. Bao, 2017. Redefining the utility of the three-isotope method. Geochim. Cosmochim. Acta, 212:16–32.

P. R. Craddock and N. Dauphas, 2011. Iron Isotopic Compositions of Geological Reference Materials and Chondrites. Geostand. Geoanalytical Res., 35(1):101–123.

P. R. Craddock, J. M. Warren, and N. Dauphas, 2013. Abyssal peridotites reveal the near-chondritic Fe isotopic composition of the Earth. Earth Planet. Sci. Lett., 365:63–76.

N. Dauphas, F.Z. Teng, N.T. Arndt, 2010. Magnesium and iron isotopes in 2.7 Ga Alexo komatiites: Mantle signatures, no evidence for Soret diffusion, and identification of diffusive transport in zoned olivine. Geochim. Cosmochim. Acta 74, 3274-3291.

C. Dalou, E. Füri, C. Deligny, L. Piani, M. C. Caumon, M. Laumonier, J. Boulliung, and M. Edén, 2019. Redox control on nitrogen isotope fractionation during planetary core formation. Proc. Natl. Acad. Sci. U. S. A., 116(29):14485–14494.

S. M. Elardo and A. Shahar, 2017. Non-chondritic iron isotope ratios in planetary mantles as a result of core formation. Nat. Geosci., 10(4):317–321.

S. M. Elardo, A. Shahar, T. D. Mock, and C. K. Sio, 2019. The effect of core composition on iron isotope fractionation between planetary cores and mantles. Earth Planet. Sci. Lett., 513:124–134.

D. G. Fraser and W. Rammensee, 1982. Activity measurements by Knudsen cell mass spectrometry—the system Fe-Co-Ni and implications for condensation processes in the solar nebula. Geochim. Cosmochim. Acta, 46(4):549–556.

D. J. Frost and C. A. McCammon, 2008. The redox state of earth's mantle. Annu. Rev. Earth Planet. Sci., 36:389–420.

A. Gargano, Z. Sharp, C. Shearer, J.I. Simon, A. Halliday, W. Buckley, 2020. The Cl isotope composition and halogen contents of Apollo-return samples. Proc. Nat. Acad. Sci. 117, 23418-23425.

R. B. Georg, A. N. Halliday, E. A. Schauble, and B. C. Reynolds, 2007. Silicon in the Earth's core. Nature, 447(7148):1102–1106.

D.H. Green, I.A. Nicholls, M. Viljoen, R. Viljoen, 1975. Experimental demonstration of the existence of peridotitic liquids in earliest Archean magmatism. Geology, 3, 11-14.

J. Guignard, G. Quitté, M. Méheut, M. J. Toplis, F. Poitrasson, D. Connetable, and M. Roskosz, 2020. Nickel isotope fractionation during metal-silicate differentiation of planetesimals: Experimental petrology and ab initio calculations. Geochim. Cosmochim. Acta, 269:238–256.

K.E.J. Hibbert, H.M. Williams, A.C. Kerr, I.S. Putchtel, 2012. Iron isotopes in ancient and modern komatiites: Evidence in support of an oxidised mantle from Archean to present. Earth Planet. Sci. Lett. 321-322, 198-207.

R. C. Hin, C. Burkhardt, M. W. Schmidt, B. Bourdon, and T. Kleine, 2013. Experimental evidence for Mo isotope fractionation between metal and silicate liquids. Earth Planet. Sci. Lett., 379:38–48.

R. C. Hin, C. Fitoussi, M. W. Schmidt, and B. Bourdon, 2014. Experimental determination of the Si isotope fractionation factor between liquid metal and liquid silicate. Earth Planet. Sci. Lett., 387:55–66.

R. C. Hin, M. W. Schmidt, and B. Bourdon, 2012. Experimental evidence for the absence of iron isotope fractionation between metal and silicate liquids at 1 GPa and 1250–1300 °C and its cosmochemical consequences. Geochim. Cosmochim. Acta, 93:164–181.

564 D. Huang and J. Badro, 2018. Fe-Ni ideality during core formation on Earth. Am. Mineral.,
565 103(10):1707–1710.

566 A. P. Kantor, I. Y. Kantor, A. V. Kurnosov, A. Y. Kuznetsov, N. A. Dubrovinskaia, M. Krisch,
567 A. A. Bossak, V. P. Dmitriev, V. S. Urusov, and L. S. Dubrovinsky, 2007. Sound wave
568 velocities of fcc Fe-Ni alloy at high pressure and temperature by mean of inelastic X-
569 ray scattering. Phys. Earth Planet. Inter., 164(1-2):83–89.

570 C. Kato, F. Moynier, M. C. Valdes, J. K. Dhaliwal, and J. M. Day, 2015. Extensive volatile loss
571 during formation and differentiation of the Moon. Nat. Commun., 6:1–4.

572 J. Kempl, P. Z. Vroon, E. Zinngrebe, and W. van Westrenen, 2013. Si isotope fractionation
573 between Si-poor metal and silicate melt at pressure-temperature conditions relevant to
574 metal segregation in small planetary bodies. Earth Planet. Sci. Lett., 368:61–68.

575 E. Kubik, J. Siebert, B. Mahan, J.B. Creech, I. Blanchard, A. Agranier, S. Shcheka, F. Moynier,
576 2021. Tracing Earth's volatile delivery with tin. J. Geophys. Res. Solid Earth, 126,
577 e2021JB022026.

578 S. van der Laan, Y. Zhang, A. K. Kennedy, and P. J. Wyllie, 1994. Comparison of element and
579 isotope diffusion of K and Ca in multicomponent silicate melts. Earth Planet. Sci. Lett.,
580 123(1-3):155–166.

581 J. Labidi, A. Shahar, C. Le Losq, V. J. Hillgren, B. O. Mysen, and J. Farquhar, 2016.
582 Experimentally determined sulfur isotope fractionation between metal and silicate and
583 implications for planetary differentiation. Geochim. Cosmochim. Acta, 175:181–194.

584 C. Lazar, E. D. Young, and C. E. Manning, 2012. Experimental determination of equi- librium
585 nickel isotope fractionation between metal and silicate from 500°C to 950°C. Geochim.
586 Cosmochim. Acta, 86:276–295.

587 C. E. Lesher, 1990. Decoupling of chemical and isotopic exchange during magma mixing.
588 Nature, 344(6263):235–237.

589 C. E. Lesher, J. Dannberg, G. H. Barfod, N. R. Bennett, J. J. Glessner, D. J. Lacks, and J. M.
590 Brenan, 2020. Iron isotope fractionation at the core–mantle boundary by
591 thermodiffusion. Nat. Geosci., 13(5):382–386.

592 J. F. Lin, V. V. Struzhkin, W. Sturhahn, E. Huang, J. Zhao, M. Y. Hu, E. E. Alp, H. kwang
593 Mao, N. Boctor, and R. J. Hemley, 2003. Sound velocities of iron- nickel and iron-
594 silicon alloys at high pressures. Geophys. Res. Lett., 30(21):1–4.

595 J. Liu, N. Dauphas, M. Roskosz, M. Y. Hu, H. Yang, W. Bi, J. Zhao, E. E. Alp, J. Y. Hu, and
596 J. F. Lin, 2017. Iron isotopic fractionation between silicate mantle and metallic core at
597 high pressure. Nat. Commun., 8:1–6.

598 Y. Liu, M. J. Spicuzza, P. R. Craddock, J. M. Day, J. W. Valley, N. Dauphas, and L. A. Taylor,
599 2010. Oxygen and iron isotope constraints on near-surface fractionation effects and the
600 composition of lunar mare basalt source regions. Geochim. Cosmochim. Acta,
601 74(21):6249–6262.

602 B. Mahan, J. Siebert, E. A. Pringle, and F. Moynier, 2017. Elemental partitioning and isotopic
603 fractionation of Zn between metal and silicate and geochemical estimation of the S
604 content of the Earth's core. Geochim. Cosmochim. Acta, 196:252–270.

605 B. Martorell, J. Brodholt, I. G. Wood, and L. Vočadlo, 2013. The effect of nickel on the
606 properties of iron at the conditions of Earth's inner core: Ab initio calculations of
607 seismic wave velocities of Fe-Ni alloys. Earth Planet. Sci. Lett., 365:143–151.

V. Matjuschkin, R.A. Brooker, B. Tattitch, J.D. Blundy, C.C. Stamper, 2015. Control and monitoring of oxygen fugacity in piston cylinder experiments. Contrib. Mineral. Petrol. 169:9.

P. McDade, B. Wood, W. Van Westrenen, R. Brooker, G. Gudmundsson, H. Soulard, J. Najorka, and J. Blundy, 2002. Pressure corrections for a selection of piston-cylinder cell assemblies. Mineral. Mag., 66(6):1021–1028.

W. F. McDonough and S. S. Sun, 1995. The composition of the Earth. Chem. Geol., 120(3-4):223–253.

F. Moynier, Q. Z. Yin, and E. Schauble, 2011. Isotopic evidence of Cr partitioning into Earth's core. Science, 331(6023):1417–1420.

O. Nebel, P. A. Sossi, J. Foden, A. Bénard, P. A. Brandl, J. A. Stammeier, J. Lupton, M. Richter, and R. J. Arculus, 2018. Iron isotope variability in ocean floor lavas and mantle sources in the Lau back-arc basin. Geochim. Cosmochim. Acta, 241:150–163.

P. Ni, N.L. Chabot, C.J. Ryan, A. Shahar, 2020. Heavy iron isotope composition of iron meteorites explained by core crystallization. Nat. Geosci. 13, 611-615.

R. A. Oriani, 1953. Thermodynamic activities in iron-nickel alloys. Acta metall., 1(4):448–454.

D. Perkins and R. Newton, 1981. Charnockite geobarometers based on coexisting gar- net—pyroxene—plagioclase—quartz. Nature, 292(5819):144–146.

C. Pinilla, A. de Moya, S. Rabin, G. Morard, M. Roskosz, M. Blanchard, 2021. First-principles investigation of equilibrium iron isotope fractionation in $Fe_{1-x}S_x$ alloys at Earth's core formation conditions. Earth Planet. Sci. Lett., 569, 117059.

F. Poitrasson, 2007. Does planetary differentiation really fractionate iron isotopes? Earth Planet. Sci. Lett., 256(3-4):484–492.

F. Poitrasson, A. N. Halliday, D. C. Lee, S. Levasseur, and N. Teutsch, 2004. Iron isotope differences between Earth, Moon, Mars and Vesta as possible records of contrasted accretion mechanisms. Earth Planet. Sci. Lett., 223(3-4):253–266.

F. Poitrasson, M. Roskosz, and A. Corgne, 2009. No iron isotope fractionation between molten alloys and silicate melt to 2000 °C and 7.7 GPa: Experimental evidence and implications for planetary differentiation and accretion. Earth Planet. Sci. Lett., 278(3- 4):376–385.

F. Poitrasson, T. Zambardi, T. Magna, and C. R. Neal, 2019. A reassessment of the iron isotope composition of the Moon and its implications for the accretion and differentia- tion of terrestrial planets. Geochim. Cosmochim. Acta, 267:257–274.

V. B. Polyakov, 2009. Equilibrium iron isotope fractionation at core-mantle boundary conditions. Science, 323(5916):912–914.

E. A. Pringle and F. Moynier, 2017. Rubidium isotopic composition of the Earth, mete- orites, and the Moon: Evidence for the origin of volatile loss during planetary accretion. Earth Planet. Sci. Lett., 473:62–70.

K. Righter and M. J. Drake, 1996. Core formation in Earth's moon, Mars, and Vesta. Icarus, 124(2):513–529.

P. Savage, F. Moynier, H. Chen, G. Shofner, J. Siebert, J. Badro, and I. Puchtel, 2015. Copper isotope evidence for large-scale sulphide fractionation during Earth's differen- tiation. Geochemical Perspect. Lett., pages 53–64.

R. Schoenberg and F. von Blanckenburg, 2006. Modes of planetary-scale Fe isotope fractionation. Earth Planet. Sci. Lett., 252(3-4):342–359.

A. Shahar, V. J. Hillgren, E. D. Young, Y. Fei, C. A. Macris, and L. Deng, 2011. High-temperature Si isotope fractionation between iron metal and silicate. Geochim. Cosmochim. Acta, 75(23):7688–7697.

A. Shahar and E. D. Young, 2020. An assessment of iron isotope fractionation during core formation. Chem. Geol., 554:119800.

A. Shahar, E. D. Young, and C. E. Manning, 2008. Equilibrium high-temperature Fe iso- tope fractionation between fayalite and magnetite: An experimental calibration. Earth Planet. Sci. Lett., 268(3-4):330–338.

A. Shahar, K. Ziegler, E. D. Young, A. Ricolleau, E. A. Schauble, and Y. Fei, 2009. Experimentally determined Si isotope fractionation between silicate and Fe metal and implications for Earth's core formation. Earth Planet. Sci. Lett., 288(1-2):228–234.

Z. D. Sharp, C. K. Shearer, K. D. McKeegan, J. D. Barnes, and Y. Q. Wang, 2010. The Chlorine Isotope Composition of the Moon and Implications for an Anhydrous Mantle. Science, 329(5995):1050–1053.

J. Siebert, A. Corgne, and F. J. Ryerson, 2011. Systematics of metal-silicate partitioning for many siderophile elements applied to Earth's core formation. Geochim. Cosmochim. Acta, 75(6):1451–1489.

E.M. Smith, P. Ni, S.B. Shirey, S.H. Richardson, W. Wang, A. Shahar, 2021. Heavy iron in large gem diamonds traces deep subduction of serpentinized ocean floor. Sci. Adv., 7, eabe9773.

C.R. Soderman, S. Matthews, O. Shorttle, M.G. Jackson, S. Ruttor, O. Nebel, S. Turner, C. Beier, M.A. Millet, E. Widom, M. Humayun, H. Williams, 2021. Heavy δ^{57}Fe in ocean island basalts: A non-unique signature of processes and source lithologies in the mantle. Geochim. Cosmochim. Acta, 292, 309-332.

P. A. Sossi, G. P. Halverson, O. Nebel, and S. M. Eggins, 2015. Combined separation of Cu, Fe and Zn from rock matrices and improved analytical protocols for stable isotope determination. Geostand. Geoanalytical Res., 39(2):129–149.

P. A. Sossi and F. Moynier, 2017. Chemical and isotopic kinship of iron in the Earth and Moon deduced from the lunar Mg-Suite. Earth Planet. Sci. Lett., 471:125–135.

P. A. Sossi, O. Nebel, M. Anand, and F. Poitrasson, 2016a. On the iron isotope composition of Mars and volatile depletion in the terrestrial planets. Earth Planet. Sci. Lett., 449:360–371.

P. A. Sossi, F. Moynier, and K. Van Zuilen, 2018. Volatile loss following cooling and accretion of the Moon revealed by chromium isotopes. Proc. Natl. Acad. Sci. U. S. A., 115(43):10920–10925.

P. A. Sossi, O. Nebel, and J. Foden, 2016b. Iron isotope systematics in planetary reservoirs. Earth Planet. Sci. Lett., 452:295–308.

P. A. Sossi, O. Nebel, H. S. C. O'Neill, and F. Moynier, 2017. Zinc isotope composition of the Earth and its behaviour during planetary accretion. Chem. Geol., 477:73–84.

F.Z. Teng, N. Dauphas, S. Huang, B. Marty, 2013. Iron isotopic systematics of oceanic basalts. Geochim. Cosmochim. Acta, 107, 12-26.

694 Y. Thibault and M. J. Walter, 1995. The influence of pressure and temperature on the metal-
695 silicate partition coefficients of nickel and cobalt in a model C1 chondrite and
696 implications for metal segregation in a deep magma ocean. Geochim. Cosmochim. Acta,
697 59(5):991–1002.

698 H. C. Urey, 1947. The thermodynamic properties of isotopic substances. J. Chem. Soc., pages
699 562–581.

700 T. Wakamatsu, K. Ohta, T. Yagi, K. Hirose, and Y. Ohishi, 2018. Measurements of sound
701 velocity in iron–nickel alloys by femtosecond laser pulses in a diamond anvil cell. Phys.
702 Chem. Miner., 45(6):589–595.

703 K. Wang and S. B. Jacobsen, 2016. Potassium isotopic evidence for a high-energy giant impact
704 origin of the Moon. Nature, 538(7626):487–490.

705 K. Wang, S. B. Jacobsen, F. Sedaghatpour, H. Chen, and R. L. Korotev, 2015. The earliest
706 Lunar Magma Ocean differentiation recorded in Fe isotopes. Earth Planet. Sci. Lett.,
707 430:202–208.

708 K. Wang, F. Moynier, J.A. Barrat, B. Zanda, R.C. Paniello, P.S. Savage, 2013. Homogeneous
709 distribution of Fe isotopes in the early solar nebula. Meteorit. Planet, Sci., 48, 354-364.

710 K. Wang, F. Moynier, N. Dauphas, J. A. Barrat, P. Craddock, and C. K. Sio, 2012. Iron isotope
711 fractionation in planetary crusts. Geochim. Cosmochim. Acta, 89:31–45.

712 K. Wang, P.S. Savage, F. Moynier, 2014. The iron isotope composition of enstatite meteorites:
713 Implications for their origin and the metal/sulfide Fe isotopic fractionation factor.
714 Geochim. Cosmochim. Acta, 142, 149-165.

715 S. Weyer, A. D. Anbar, G. P. Brey, C. Münker, K. Mezger, and A. B. Woodland, 2005. Iron
716 isotope fractionation during planetary differentiation. Earth Planet. Sci. Lett.,
717 240(2):251–264.

718 S. Weyer, D.A. Ionov, 2007. Partial melting and melt percolation in the mantle: The message
719 from Fe isotopes. Earth Planet. Sci. Lett., 259, 119-133.

720 H. M. Williams, A. Markowski, G. Quitté, A.N. Halliday, N. Teutsch, S. Levasseur, 2006. Fe
721 isotope fractionation in iron meteorites: New insights into metal-sulphide segregation
722 and planetary accretion. Earth Planet. Sci. Lett. 250, 486-500.

723 H. M. Williams, B. J. Wood, J. Wade, D. J. Frost, and J. Tuff, 2012. Isotopic evidence for
724 internal oxidation of the Earth's mantle during accretion. Earth Planet. Sci. Lett., 321-
725 322:54–63.

726 B. J. Wood, M. J. Walter, and J. Wade, 2006. Accretion of the Earth and segregation of its core.
727 Nature, 441(7095):825–833.

728 Y. Xia, E. Kiseeva, J. Wade, and F. Huang, 2019. The effect of core segregation on the Cu and
729 Zn isotope composition of the silicate Moon. Geochemical Perspect. Lett., pages 12–
730 17.

731 H. Yang, J.F. Lin, M.Y. Hu, M. Roskosz, W. Bi, J. Zhao, E.E. Alp, J. Liu, J. Liu, R.M.
732 Wentzcovitch, T. Okuchi, N. Dauphas, 2019. Iron isotopic fractionation in mineral
733 phases from Earth's lower mantle: Did terrestrial magma ocean crystallization
734 fractionate iron isotopes? Earth Planet. Sci. Lett. 506, 113-122.

735 E.D. Young, 2021. Revisiting the Wasson fractional crystallization model for IIIAB iron
736 meteorites with implications for the interpretation of their Fe isotope ratios. Meteorit.
737 Planet. Sci. 1-10.

G. Zellars, S. Payne, J. Morris, and R. Kipp, 1959. The activities of iron and nickel in liquid Fe-Ni alloys. Trans. Metall. Soc., 215:181–185.

Supplementary materials

Isotopic equilibrium

In each experiment, metal coalescence into a single metal sphere of roughly 1 mm diameter in the center of the capsule was observed as a result of achievement of superliquidus temperatures during sufficient time duration to allow elemental and isotopic equilibrium. Fig. 5 represents backscatter electron images of typical run products. Silicate phases of the experiments of the time series (Fig. 5a-d) show skeletal olivine (dark gray dendrites) due to MgO enrichment and slow quenching rates, but their electron density is homogeneous. A thin, dense ring of roughly 30 μm between the silicate and the capsule constitutes the transition zone and no Fe was detected with EDX in the capsule beyond this zone. The capsule of run E382 (Fig. 5d) appears to have broken during the run and some silicate material can be observed in the fracture. This may be the reason for the negative isotopic fractionation factor measured, caused by light Fe loss from the capsule resulting in a heavier Fe measured in the silicate. The metal phases (Fig. 5e-f) are also homogeneous in their elemental composition as determined by electron microscopy. Fig. 6 and 7 present additional EDX measurements for a silicate and a metal part. Major element compositions of the two phases are consistent across the samples, demonstrating chemical homogeneity. Fig. 8 shows Fe isotopic fractionation results for experiments of the time series carried at 2 GPa, 1873 K and with 30 *wt.* % Ni in the metal phase. Up to 30 minutes, there is no resolvable change in the fractionation factor suggesting achievement of equilibrium, which is consistent with strong evidence of full equilibration from petrographic observations and EDX measurements previously described. As mentioned above, the 60 min experiment may have interacted with the exterior of the capsule, causing a very

762 negative fractionation factor. Our results support isotopic equilibrium achievement within a few
763 minutes at the conditions of our experiments.

764 Therefore, primary petrological observations and EDX measurements—from 5 to 60
765 minutes run durations—showed the metal and silicate phases of the experiments of this study
766 to be fully molten with quench textures and, most importantly, chemically homogeneous which
767 is crucial for achievement of isotopic equilibrium.

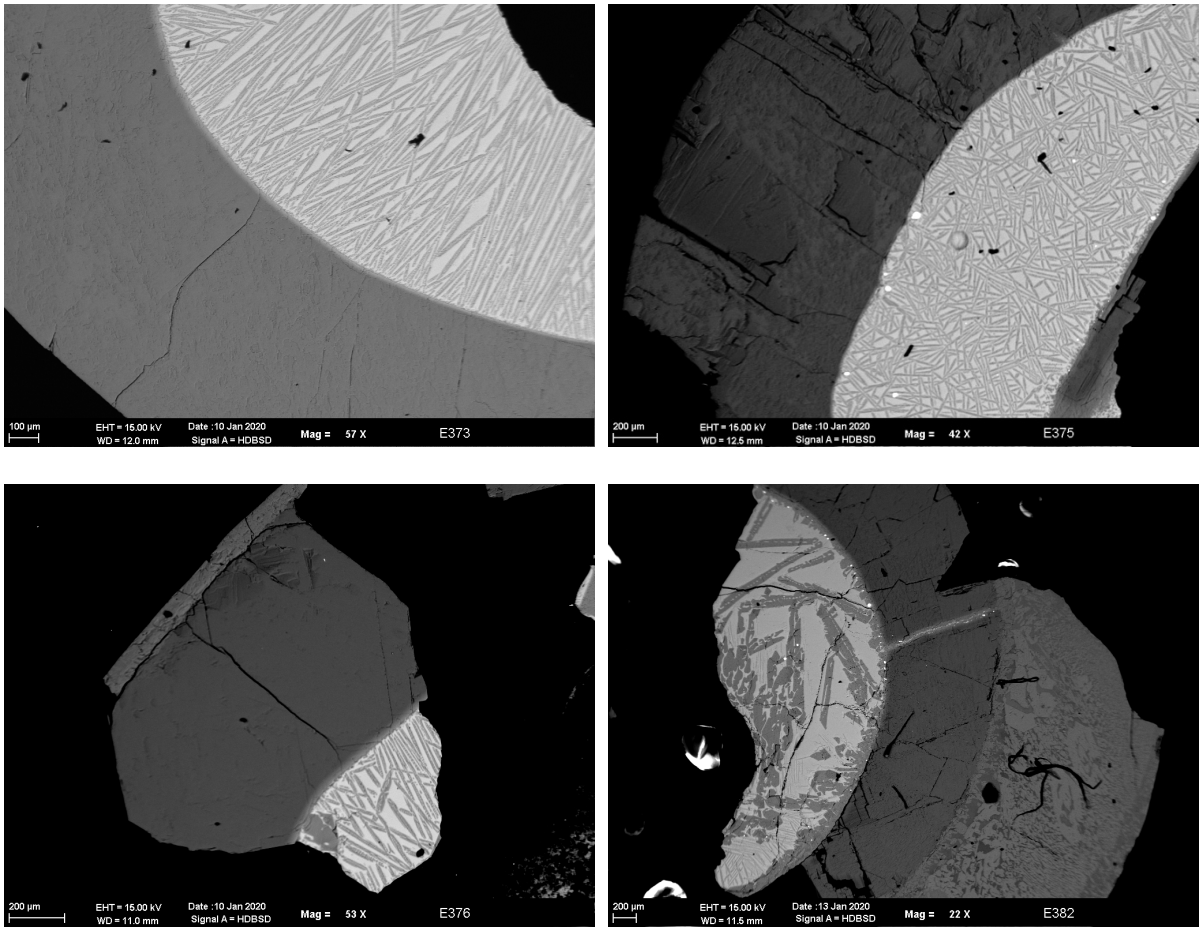

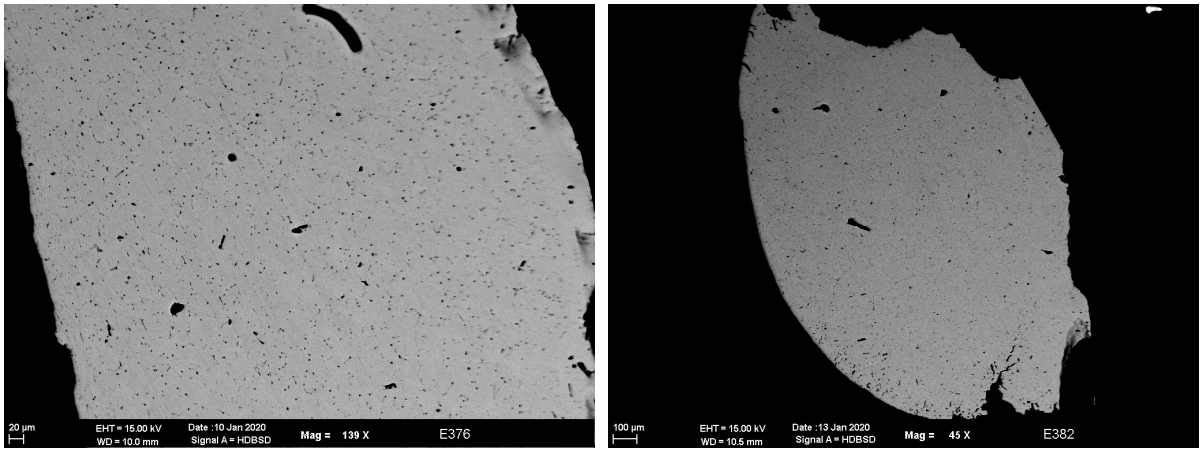

Figure 5: Backscatter electron images of typical run products. The first four images represent the silicate phase attached to its capsule—such that the silicate–capsule boundary is visible—for all experiments of the time series performed in single-crystal MgO capsules at 2 GPa and 1873 K and 30 *wt.*% Ni in the metal part. The last two images represent typical metal phases. **a.** Backscatter electron (BSE) image of the silicate of run E373. **b.** BSE image of the silicate part of run E375. **c.** BSE image of the silicate phase of run E376. **d.** BSE image of the silicate of run E382. **e.** BSE image of the metal of run E376. **f.** BSE image of the metal phase of run 382.

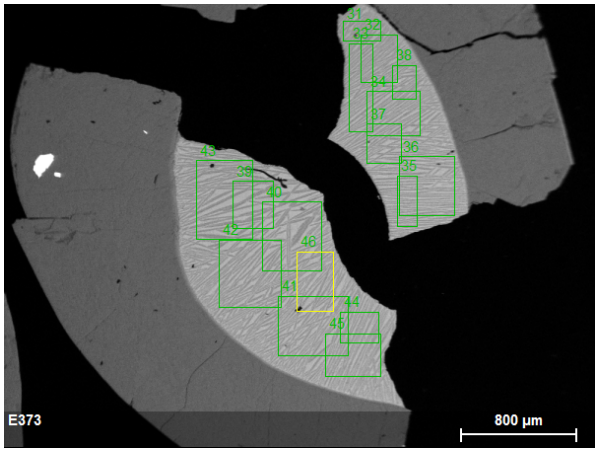

Norm. mass percent (%)

Spectrum	O	Na2O	MgO	Al2O3	SiO2	CaO	TiO2	FeO	K2O
31	0.00	2.04	24.71	14.04	38.55	10.49	0.99	8.86	0.32
32	0.00	2.07	24.68	14.14	38.64	10.46	0.90	8.87	0.24
33	0.00	1.98	24.31	14.32	38.67	10.60	0.93	8.96	0.23
34	0.00	2.06	24.51	14.12	38.74	10.61	0.93	8.78	0.24
35	0.00	1.99	23.86	14.38	38.87	10.84	0.86	8.95	0.23
36	0.00	2.01	23.76	14.44	38.76	10.93	0.98	8.86	0.26
37	0.00	1.94	24.81	14.00	38.69	10.53	1.00	8.77	0.26
38	0.00	1.94	24.68	13.95	38.80	10.59	0.96	8.83	0.24
39	0.00	1.96	24.45	14.21	38.83	10.52	0.95	8.92	0.17
40	0.00	2.03	24.75	14.09	38.78	10.48	0.88	8.83	0.17
41	0.00	1.93	24.27	14.18	38.94	10.68	0.93	8.90	0.17
42	0.00	1.98	24.35	14.28	38.74	10.63	0.97	8.85	0.20
43	0.00	1.94	25.18	13.94	38.69	10.25	0.91	8.89	0.19
44	0.00	1.96	24.76	14.08	38.70	10.41	0.88	8.99	0.21
45	0.00	1.90	24.16	14.41	38.84	10.80	0.81	8.85	0.23
46	0.00	1.98	24.13	14.29	38.85	10.62	0.97	8.98	0.17
Mean value:	0.00	1.98	24.46	14.18	38.76	10.59	0.93	8.88	0.22

Figure 6: Energy-dispersive X-ray spectroscopy (EDX) measurements on the silicate part of run E373 proving chemical homogeneity of the quenched melted silicate phase, even after 5 minutes run duration.

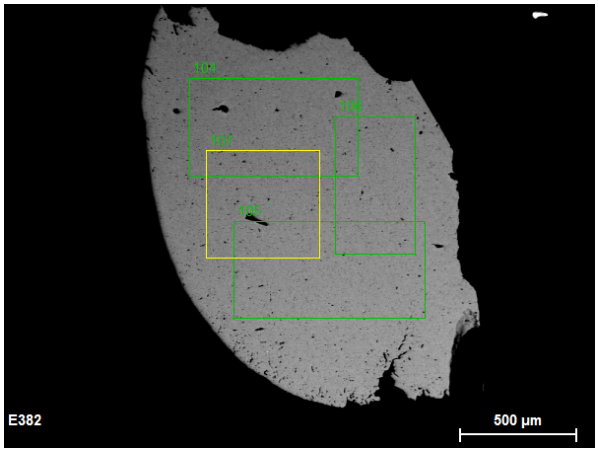

Norm. mass percent (%)

Spectrum	O	Si	P	S	Fe	Ni
104	-	0.10	0.13	0.36	68.58	30.84
105	-	-	-	0.31	68.69	30.99
106	-	0.14	-	0.35	68.59	30.92
107	1.70	0.14	-	0.31	67.64	30.20
Mean value:	1.70	0.12	0.13	0.33	68.38	30.74
Sigma:	0.00	0.02	0.00	0.03	0.49	0.36
Sigma mean:	0.00	0.01	0.00	0.01	0.25	0.18

Figure 7: Energy-dispersive X-ray spectroscopy (EDX) measurements on the metal part of run E382 presenting chemical homogeneity of the quenched melted metal.

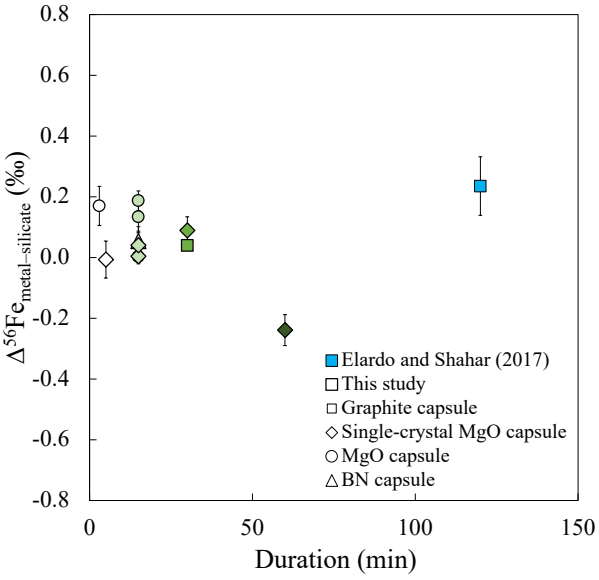

Figure 8: $\Delta^{56}Fe_{metal-silicate}$ as a function of time duration for experiments containing 30 *wt.*% Ni in the metal fraction at 2 GPa and 1873 K. Experiments from this study are represented with a thick line symbol, experiment from Elardo and Shahar (2017) is represented with a blue thin line symbol. Graphite encapsulated experiments are represented by a square, experiments with single-crystal MgO capsules by a diamond, circles represent crushable MgO experiments, and BN encapsulated experiments are represented by a triangle. Experiments are color coded according to their equilibrium temperature (same color code as Fig. 1b).

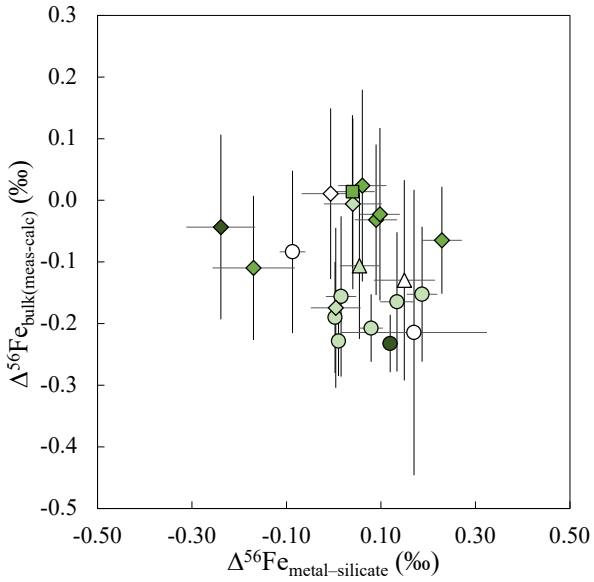

Figure 9: $\Delta^{56}Fe_{bulk}$ corresponding to the difference between the measured Fe isotopic composition of the experimental starting material and the calculated bulk composition of the experiment by mass balance, as a function of $\Delta^{56}Fe_{metal–silicate}$. $\Delta^{56}Fe_{bulk}$ being an indicator of Fe loss during experiments, this figure demonstrates that there is no systematic effect of the moderate Fe loss occurring in our experiments on the Fe isotopic fractionation factor. This figure also shows that single-crystal MgO capsules systematically led to reduced Fe loss with respect to BN and crushable MgO capsules, as their $\Delta^{56}Fe_{bulk}$ is closer to zero.

On the variability of isotopic fractionation data in metal–silicate experiments

To further investigate the quality of our data, it was compared to those obtained from previous metal–silicate isotopic fractionation experiments. As scatter can be expected from experimental data resulting from random errors in the experimental preparation and run, such comparison allows to assess if the data from this study shows enhanced scatter or if it shares the same magnitude of scattering as in other studies. When compared to the scatter/amu of previous studies using the same method (Table 2), we find that the new data reported in this study is scattered to the same order of magnitude as other data sets, which is characteristic of the combined piston cylinder – MC-ICPMS approach. In this compilation, the scatter was determined using experiments sharing the same P, T and composition, and experiments with distinct parameters were only included if such a parameter was reported to have no effect on the fractionation factor.

Table 2: Comparison of scatter/amu for other metal–silicate isotopic fractionation studies. n corresponds to the number of experiments in each data set used for scatter determination.

	Element	Notation	n	Scatter[1] (‰)	Scatter/amu[1] (‰)	Scatter[2] (‰)	Scatter/amu[2] (‰)
This study	Fe	$\Delta^{56/54}$Fe	22	0.47	0.24	0.53	0.27
Elardo and Shahar (2017)	Fe	$\Delta^{57/54}$Fe	8	0.32	0.11	0.43	0.14
Hin et al. (2012)	Fe	$\Delta^{57/54}$Fe	10	0.33	0.11	0.84	0.28
Poitrasson et al. (2009)	Fe	$\Delta^{57/54}$Fe	4	0.09	0.03	0.41	0.14
Kubik et al. (2021)	Sn	$\Delta^{122/118}$Sn	2	0.28	0.07	0.34	0.08
Mahan et al. (2017)	Zn	$\Delta^{66/64}$Zn	9	0.54	0.27	0.63	0.31
Hin et al. (2014)	Si	$\Delta^{30/28}$Si	5	0.46	0.23	0.66	0.33

[1] Scatter corresponding to the maximum difference between data points of identical PT conditions excluding their error.
[2] Scatter corresponding to the maximum difference between data points of identical PT conditions including 2 S.D.